MIT Open Access Articles

Quasi-coherent fluctuations limiting the pedestal growth on Alcator C-Mod: experiment and modelling

PSFC/JA-14-37

Quasi-Coherent Fluctuations Limiting
the Pedestal Growth on Alcator C-Mod:
Experiment and Modeling

Diallo, A.[1], Hughes, J.W., Baek, S-G., LaBombard, B., Terry, J., Cziegler, I.[2], Hubbard, A., Davis, E., Walk, J., Delgado-Aparicio, L.[1], Reinke, M.L., Theiler, C., Churchill, R.M., Edlund, E.M.[1], Canik, J.[3], Snyder, P.[4], Greenwald, M., White, A., the Alcator C-Mod Team

[1]Princeton Plasma Physics Laboratory
[2]Center for Energy Research, University of California, San Diego
[3]Oak Ridge National Laboratory
[4]General Atomics

December 2014

Plasma Science and Fusion Center
Massachusetts Institute of Technology
Cambridge MA 02139 USA

Quasi-Coherent Fluctuations Limiting the Pedestal Growth on Alcator C-Mod: Experiment and Modeling

A. Diallo[1], J.W. Hughes[2], S-G. Baek[2], B. LaBombard[2], J. Terry[2], I. Cziegler[3], A. Hubbard[2], E. Davis[2], J. Walk[2], L. Delgado-Aparicio[1], M.L. Reinke[2], C. Theiler[2], R.M.Churchill[2], E.M. Edlund[1], J. Canik[4], P. Snyder[5], M. Greenwald[2], A.White[2], and the Alcator C-Mod team

[1]Princeton Plasma Physics Laboratory, Princeton University, NJ, USA.
[2]Plasma Science and Fusion Center, MIT, Cambridge, MA, USA.
[3]Center for Energy Research, University of California, San Diego, CA, USA.
[4]Oak Ridge National Laboratory, Oak Ridge, TN, USA.
[5]General Atomics, San Diego, CA, USA.

E-mail: `adiallo@pppl.gov`

Abstract.
    Performance predictions for future fusion devices rely on an accurate model of the pedestal structure. The leading candidate for predictive pedestal structure is EPED, and it is imperative to test the underlying hypothesis to further gain confidence for ITER projections. Here, we present experimental work testing one of the EPED hypothesis, namely the existence of a soft limit set by microinstabilities such as the kinetic ballooning mode (KBM). This work extends recent work on Alctor C-Mod [Diallo, *et al.*, Phys. Rev. Lett., **112**, (2014), 115001], to include detailed measurements of the edge fluctuations and comparisons of edge simulation codes and experimental observations.

1. Introduction

Future fusion device performance prediction relies on a theoretical understanding of the edge plasma parameters in high performance regimes. A successful predictive model based on core transport theory has shown that the core fusion performance is tightly correlated with the pressure at the top of the edge barrier region [1]. This barrier is spontaneously generated in high performance (H-mode) operation in tokamaks, and is localized in the last few centimeters of the confined plasma. In a nutshell, it is generally accepted that optimizing the edge pedestal will lead to maximum core fusion performance. This is a strong motivation for establishing and validating edge predictive models. At present the leading model is EPED [2] which has some success in predicting the pedestal height and width: two important parameters defining the edge of confined plasmas in future tokamak devices. The EPED model has two hypotheses: (1) the pedestal height is limited by the peeling-ballooning (P-B) mode, which triggers edge-localized modes (ELMs) and (2) the pedestal pressure gradient, defined as the pedestal height-to-width ratio, is limited by the onset of a microinstability, namely, the kinetic ballooning mode (KBM), which contributes to enhanced transport.

EPED successfully predicted the pedestal parameters on multiple experimental devices [2], including Alcator C-Mod [3]. Motivated by this success, we examined the role of edge fluctuations in limiting the pressure pedestal and performed gyrokinetic calculations to support the observations. Note that previous gyrokinetic calculations on MAST [4, 5] and NSTX [6] have shown the co-existence of microtearing and KBM instabilities. These two microinstabilities helped form a new physical picture during the pedestal evolution, whereby the KBMs are found to limit the steep pressure and density gradients in the pedestal region. Microtearing modes, on the other hand, dominate regions of shallower pressure gradients until these modes are supplanted by KBMs when the pressure gradient increases. This picture, as well as key EPED hypothesis, need to be supported by data from a broader range of H-mode plasmas.

More importantly, extensive turbulence diagnostics can provide key tests of the edge microinstabilities at play. For instance, the KBM mode can be considered a soft limit as it clamps the pressure gradient, letting the pedestal height and width evolve until the ultimate (P-B) limit is reached. This soft limit motivated recent experimental efforts to focus on observing the onset of this mode between ELMs. On the DIII-D tokamak, high frequency coherent (HFC) modes were observed in QH-mode plasmas with some features qualitatively similar to those expected for KBMs [7]. These modes have characteristics of a long poloidal wavelength, and low frequency band of fluctuations were observed during ELM recovery. It was also shown that these fluctuations' saturation are well correlated with the electron pressure gradient [8], qualitatively consistent with KBMs. Other experiments on DIII-D indicated the onset of coherent modes on the BES diagnostic shortly after L-H transition [9], which appears to slow down the evolution of the pressure gradient leading up to the first ELM. Moreover, the pressure gradient is shown to be close to the KBM critical gradient. On Alcator C-Mod, detailed studies between type-I ELMs have shown quasi-coherent fluctuations (QCF) that appear to grow as the pedestal temperature gradient increases and saturates preceding an ELM [10]. These QCFs are different from the quasi-coherent modes (QCM) observed in enhanced-D_α H-mode discharges in C-Mod.

Here, we describe the profile and fluctuation measurements performed in the pedestal to identify the edge fluctuations responsible for limiting the pedestal evolution

in Alcator C-Mod. Section 2 details the experimental conditions, which provided type I ELMs and summarizes the global plasma parameters. In section 3 various edge fluctuations measurements point to quasi-coherent fluctuations being localized in the pedestal. Section 4, analyses of the edge stability using the MHD and gyro kinetics approaches are described and results are found to support the experimental observations. Finally, a summary and discussion of the impact of these results are provided in section 5

2. Edge Profile Characterization

Experiments were performed on the Alcator C-Mod tokamak [11] with major radius $R = 67$ cm and minor radius $a = 21$ cm, with typical magnetic field strength ranging from 2.6 T to 8.0 T, and high densities ($< 10^{21}$ m^{-3}). The ELMy H-mode discharges presented here were produced using auxiliary heating from Ion Cyclotron Range of Frequency (ICRF) minority heating [12]. These discharges are typically achieved when Alcator C-Mod is operated with an equilibrium shape consisting of a low elongation ($\kappa \sim 1.4 - 1.5$) and high lower triangularity ($\delta_l \sim 0.8$). In addition, the outer-divertor leg is steered to the more closed flat plate of the divertor floor (see fig. 1(a)). Such divertor configuration, in combination with a reduced fueling yields lower than usual pedestal collisionality ($\nu_{ped}^* < 2$). In the experimental results as described here, the ELMy regime was obtained with plasma current (I_p) around 900 kA, and magnetic field at 5.4 T.

Electron density and temperature were measured using the Thomson scattering system [13]. Ion profiles were provided using X-ray crystal spectrometer [14] for the core to near pedestal top profiles of the ion temperature, and the gas puff charge-exchange(CXRS) system [15] for the edge ion temperature. To enhance the temporal resolution of the electron temperature evolution between ELMs, electron cyclotron emission(ECE) measurements [16] have been made. For experimental characteristic contrasts, figure 1(b -e) displays the enhanced D_α (EDA) regime (see ref. [17] for details of this regime) commonly observed in a high collisionality regime as well as the ELMy regime. As discussed above, the ELMy regime is readily achieved with lower overall line-averaged density associated with lower pedestal collisionality than those of EDA regimes.

Figure 2 displays the temperature profiles for a characteristic ELMy discharge. These profiles are obtained using the Thomson scattering system [13] for radial profiles of the electron temperature, the X-ray crystal spectrometer(XCS) [14] for the core to near pedestal top profiles of the ion temperature, and the gas puff charge-exchange(CXRS) system [15] for the edge ion temperature. This figure shows excellent agreement between the ion temperature obtained by the CXRS and XCS diagnostics (Note that the discharge numbers, although different, represent similar plasma discharges.) Moreover, figure 2 shows edge temperature equilibration ($T_e = T_i$ in the pedestal region) between ions and electrons. Note that due to mapping uncertainties, the possibility of a radial shift between the T_e and T_i of a few mm cannot be excluded. Displayed on this figure is the location of the electron cyclotron emission (ECE) measurements [16] providing the fast temporal T_e measurements, which is used in the section below to investigate the inter-ELM profile evolution.

The top panel of figure 3 shows profiles of $T^{B^{5+}}$ and E×B obtained with the gas puff CXRS diagnostic. Studies with a synthetic diagnostic, which simulate the effect of a finite width of the optical chords and a finite emission volume generated by

the gas puff, reveal that instrumental effects are rather important in these pedestals. Indeed, the red profiles in the bottom panel 3 show estimates of the "raw" uncorrected profiles, obtained with the synthetic diagnostic combined with an iterative inversion procedure. This suggests that the E_r (via E×B) well obtained this way is substantially deeper than the uncorrected one [18]. Note that the E_r (and associated $V_{E \times B}$) well has a narrow radial width of ∼4 mm consistent with the pressure pedestal width.

Finally, figure 4 depicts the evolution of the intrinsic impurity in the tokamak. In figure 4(a), a top view of Alcator C-Mod is displayed showing the AXA array [19, 20], which observes the outboard half of the plasma with a spatial resolution of ∼ 1 cm. This array measures the impurity radiations from which an emissivity profile is obtained as shown in figure 4(b-d). More specifically, figure 4(b) depicts the pedestal overall emissivity during two ELM cycles. Note that from the spatial and temporal variations of the local emissivities, a specific impurity density profile can be obtained. Admittedly, such unfolding has not been performed here (mostly due to the need to know with accuracy the composition of the intrinsic impurity content), but it suffices to say that the impurity emissivity corresponds to a measure of the impurity density. Hence, figure 4(c-d) shows radial profiles for each ELM cycle clearly demonstrating that ELMs contribute to the flushing of the impurity mostly accumulated at the pedestal top (similar results were reported on DIII-D in Ref. [21]). This impurity accumulation at the pedestal top is also evidenced in figure 4(b), which might suggest near constant intrinsic impurity influx. As will be seen later in this paper, the impurity content appears to be the only plasma parameter increasing monotically leading up to an ELM.

3. Role of fluctuations in limiting the pedestal

To better understand the role of fluctuations in the pedestal dynamics, we investigate both local and global fluctuations during the ELM cycle. The main diagnostics used to probe the inter-ELM fluctuations are the phase contrast imaging (PCI), the O-mode reflectometer, the gas puff-imaging, and the magnetic probes systems. Measurements from these diagnostics allow both global and local analyses of the inter-ELM fluctuations, which provide the necessary ingredients for determining correlations between the onset of fluctuations and inter-ELM pedestal evolutions.

The PCI diagnostic provides, along 32 vertical chords, measurements of the line-integrated density fluctuations [22]. Shown in figure 5 is the spectrogram of the fluctuations between ELMs as measured using the PCI system. Characteristic inter-ELM fluctuations near 300 kHz are clearly observed to begin and to last until the next ELM. Since the PCI measurements are line-integrated sampling both edge and core fluctuations, radial localization of the turbulence remains unclear. Figure 6 displays the spectrum $S(k_R, f)$ as a function of frequency and major radius wavenumber. Beside the broadband fluctuations in this figure, two coherent peaks at $k_R = \pm(1.5 \pm 0.5)$ cm^{-1} are observed from which a phase velocity (ω/k) of ±12 km/s is determined.

Further analysis of the PCI radial profile of intensity is shown in figure 7. More specifically, this figure displays the integrated inter-ELM intensity of the PCI fluctuations between 270 kHz and 300 kHz as a function of radius. Panels (a)-(d) of figure 7 clearly show an increase of both the amplitude of the radial structure and of the contrast ratio $(I_{max} - I_{min})/(I_{max} + I_{min})$, where I is the intensity of the fluctuations between 270 kHz and 300 kHz. In addition, there is a saturation of the radial structure amplitude. Furthermore, from figure 7, one can see that while

the mode amplitude grows and the contrast ratio increases prior to saturation, the mode appears to be "seeded" at larger major radius and then spreads to smaller major radius. This suggests that the poloidal extent of the mode increases as the mode grows. Assuming that the fluctuations are edge localized, k_θ would have a large contribution in k_R (this is the projection of k_θ onto the the PCI measurement plane). In addition, an increasing global extent means that the vertical extent of the mode grows as it will be shown later in this section. Since PCI samples both the top and bottom of the plasma, it is reasonable to write the detected signal as the sum of two counter-propagating sine waves $|\sin(k_R R+\omega t)+\sin(k_R R-\omega t)|^2$, which is proportional to $\cos(2k_R R)$. This suggests that the detected signal amplitude should have a radial structure of $2k_R$. This simple assumption appears to yield a wavelength in agreement with the radial structure in figure 7. While this is not a definite proof, it seems reasonable and will become obvious when other diagnostic results are considered in the analysis.

To improve radial localization of the QCF, we used the O-mode multi-channel fixed reflectometer system to probe the edge electron density fluctuations [23]. Figure 8(a) indicates the fixed frequencies with associated density cutoff layers. While the absolute density fluctuation level was difficult to assess in this experiment, the complex signals from each channel sampling the edge density provide measurements of the fluctuation characteristics at corresponding radii. Figure 8(b)-(c) displays the spectrogram of the complex signals between ELMs. It is observed that the channels probing the region of steep density exhibit QCFs that increase after ELM crashes (these QCFs are also observed in the PCI spectrogram as discussed above). The channel probing the pedestal top, on the other hand, does not display any QCF spectral features, suggesting for the time window presented that the QCFs are localized below the pedestal top in the density steep gradient region, which is typically 5mm in width. Note that this width is similar to the E_r width shown in figure 3.

The 2D measurements of the edge fluctuations are performed using the HeI gas-puff imaging (GPI) system [24]. The GPI views the low-field side spanning a 2D cross-section area of 3.5 cm (radial) by 3.9 cm (poloidal). The collected HeI emission ($\lambda = 587.6$ nm) is detected using an array of avalanche photodiodes sampled at 2 MHz. Figure 9 (a)-(c) shows the density fluctuation measurements represented as the conditional spectrum ($S(k_\theta|f)$) during the inter-ELM phase indicating that the onset and subsequent saturation of QCF. In addition to the QCF in frequency domain (~ 300 kHz), these spectra exhibit a quasi coherent fluctuation in wavenumber near $k_\theta = 0.8$ rad/cm. The QCF propagates in the electron diamagnetic direction in the laboratory frame. Based on the coherent features, a radial profile of the QCF has been obtained which is shown in figure 9(d), indicating that the QCF is radially localized over a narrow layer of full-width at half maximum of 5 mm. Note that due to uncertainties in the spatial and magnetic equilibrium reconstructions, the peak location remains unknown to within 0.5 to 1 cm in the pedestal region. Work is currently underway to better determine the spatial registration in the pedestal and will be published in a future paper.

For a complete characterization, we investigate the magnetic component–$\tilde{B}_\theta$ – associated with edge density fluctuations presented above. Such characterization is performed using a double-head magnetic probe positioned at 2 cm from separatrix. The two magnetic heads are separated poloidally by 5 mm enabling the resolution of the poloidal wavenumber spectrum. Figure 10 displays the inter-ELM magnetic $\tilde{B}_\theta$ fluctuations clearly showing (in panel (b)) the onset of the QCFs. This is further

highlighted in panel(c) when the integrated power over the frequency band (200 and 500 kHz) shows an increase followed by a saturation of the integrated power. Combined with panel (d), which shows the pedestal electron temperature as measured using the ECE diagnostic, we observed an increase of the edge temperature followed by the onset of the mode (see panel (c)). Once this mode is excited, the pedestal temperature saturates (stops evolving) until the next ELM. During the inter-ELM phase, a slight increase of the line-integrated density (panel (e)) is observed, suggesting that electron density does not provide the threshold for the onset of the mode. (Note that the Thomson scattering density and temperature measurements were too slow to resolve the inter-ELM density and temperature evolutions.) Combining density and temperature at the pedestal, however, the inter-ELM fluctuations are presented in terms of the electron β at the pedestal in panel (f) for comparison with simulations. Note it is customary to test the sensitivity of simulation results with β for KBMs.

From the double-head probe, we display in figure 11 the poloidal wavenumber $\tilde{B}_\theta$ spectra during the inter-ELM phase. Early in the inter-ELM phase, as indicated using the vertical markers in figure 11, a broadband wavenumber structure is observed, which later through the ELM cycle becomes coherent in frequency and wavenumber (see figure 11(e) -(f)). The poloidal wavenumber k_θ ranges between 0.6 and 0.7 rad/cm yielding a $k_\theta \rho_s \sim 0.04$ (corresponding to a toroidal mode number n=10), propagating with phase velocity of $\sim +30$ km/s in the electron diamagnetic direction in the laboratory frame. Note that the spatial registration accuracy of the QCF relative to the $V_{E \times B}$ remains unknowns. However, assuming that the observed QCF is located in the minimum of the radial electric field well and accounting for the instrumental effects of the CXRS diagnostic and the "barberpole" effect ‡, we determine QCF appears to be propagating with a $V_{phase} = -2 \pm 10$ km/s. Note that using the uncorrected $V_{E \times B}$ profile, the QCF is definitely propagating in the electron direction, while using the corrected profile which accounts for the instrument effects the QCF is consistent with a propagation in the ion diamagnetic direction.

To reconcile the wavenumber measurements from the diagnostics covering the poloidal direction, figure 12 summarizes the expected k_θ as a function of vertical position. In this figure, the poloidal wavenumbers obtained from PCI, GPI, and magnetic probes are plotted as a function of vertical separation. The solid line represents the expected result for a field-aligned perturbation. Figure 12 indicates agreement between the various wavenumber measurements and suggests an instability with vertical/poloidal extent.

4. Edge modeling

In this section, we analyze the edge stability using MHD and gyrokinetics. EPED, the leading model for predicting the pedestal structure, hypothesizes that in addition to a hard limit that triggers ELMs, a soft limit exists which regulates the edge transport. This transport is generated by the KBM. Below, we concentrate on the properties of edge micro instabilities.

Figure 13 displays the peeling ballooning stability diagram and the infinite-n ballooning stability boundary late in the ELM cycle. The experimental operation

‡ This effect manifests itself when measuring the poloidal velocity in the laboratory frame and the plasma is toroidally rotating. This apparent poloidal velocity in the laboratory frame is $V_{pol}^* = V_{pol}$ - $V_{tor} \tan(\alpha) + V_{phase}$, where α is the pitch angle, V_{tor} is toroidal velocity, and V_{phase} is the phase velocity of a mode.

point is represented by the cross-hair. As shown in this figure, the experimental point is near the infinite-n ballooning stability and peeling ballooning limit. Note that KBM growth rates become very large as the infinite-n ideal ballooning boundary is approached [25, 26]. As such, ideal MHD ballooning mode calculations are often used as a proxy for the violent onset of KBM instabilities and the associated stiff transport response.

In addition to MHD mode calculations, local linear gyrokinetic calculations have been performed using GS2 in the pedestal region. GS2 calculations in the pedestal region have been performed on NSTX [6, 27] and MAST [5] to show that both micro tearing modes and KBM coexist.

Figure 14 displays the growth rate (a) and real frequency (b) as a function of normalized wavenumber. This calculation was performed in the steep gradient region at $\psi_n = 0.98$ and indicates that there are two modes (electron and ion). At low $k_\theta \rho_s$, namely, ~ 0.03, the growth rate peaks with a positive real frequency indicating an ion directed mode. Note that similar calculations at $\psi_n = 0.95$ and $\psi_n = 0.96$ indicate no peak in the growth rate instability for $k_\theta \rho_s \leq 0.2$. At higher $k_\theta \rho_s$, an electron mode is dominant. This mode is not observed with the diagnostics on hand. Based on the wavenumber, the ion mode peaks at $k_\theta \rho_s \sim 0.03$, which is in agreement with the observed $k_\theta \rho_s$ of 0.04. To test the scaling of this mode with with edge parameters, a scan in β' and magnetic shear was performed as shown in figure 14(c) and (d). In this figure, the experimental operating point is labeled with a white cross, which shows that the point lies in the unstable region. This sensitivity in β' and magnetic shear indicates that this mode has the same feature as expected by KBM stability. Furthermore, the red line in figure 14(c)-(d) represents the infinite-n ideal MHD calculations, which confirms it is operating near the KBM threshold. Both infinite-n and gyrokinetic calculations suggest that the experimental point later in the ELM cycle is near the KBM threshold with $k_\theta \rho_s \sim 0.03$ and propagation direction in the plasma frame in support with observations in the section above.

5. Summary and Discussion

Detailed studies of the inter-ELM pedestal evolution with associated fluctuations were performed on Alcator C-Mod. We presented direct observations of quasi-coherent fluctuations during the type I inter-ELM phase with density and magnetic signature. Furthermore, the coherent fluctuations are shown to clearly appear during an increase of the edge temperature, which in this case can be related to the edge temperature gradient. Once the coherent fluctuations are turned on, the edge temperature saturates as well as the coherent fluctuations suggesting that the fluctuations enhance the edge transport limiting the growth of the edge temperature. Characterization of these quasi-coherent fluctuations (QCF) in frequency and wavenumber show that the QCF propagates in a direction non inconsistent with propagation in the ion diamagnetic direction in the plasma frame with $k_\theta \rho_s \sim 0.04$. In addition, the QCF is of a global nature as it is observed by multiple diagnostics all of which provide wave numbers in agreement with the assumption that the fluctuations are field aligned. Overall, these QCFs appear to be consistent with a soft limit of the edge pedestal limiting the temperature gradient with characteristics compatible with KBM.

Using edge modeling, further investigations of these QCFs are performed. Analysis using ELITE showed that the pedestal is near the peeling-ballooning and KBM stability limits. This analysis was extended to local linear gyrokinetics analysis

using GS2, which indicates that that steep gradient is near the KBM threshold and the calculated dominant mode has wavenumber and propagation direction in agreement with observation. This provided confidence that the QCFs have the same characteristics as KBM.

While there is some confidence that QCFs have the same characteristics as KBM, several questions remain unanswered. Namely, it is generally thought that KBMs are turbulent modes and therefore of large spectral width. QCFs are shown to be quasi-coherent with 10% of spectral width. Work is in progress to generate nonlinear simulations using gyrokinetic codes and provide comparison of the spectral features with observations. There are no existing nonlinear gyrokinetics calculations in the pedestal as they are computer intensive. However, gyrofluid calculations with core plasma parameters (see Ref. [28]) have shown that in the nonlinear saturated state KBMs are coherent in spectral feature. In addition to resolving the spectral features of KBM, it is worth pointing out that a correlation between temperature and QCF amplitude evolution cannot exclude resistive pressure driven modes such as resistive ballooning modes. At present, the ballooning nature of the QCFs are difficult to confirm as that would require high-field side measurements.

In the context of other observations of such QCFs, we note that the washboard modes observed in JET [29] between ELMs share some features with the QCFs observed in Alcator C-Mod. Previous results on DIII-D using the BES data showed the existence of a coherent mode that turned on after the L-H transition [9]. This increase/turn-on appears to correlate with the slow down of ∇P_e. Furthermore, the experimental ∇P_e was shown to track the KBM calculated ∇P_e right after the L-H transition. Finally, we note that similar recent observations on DIII-D indicate that QCFs appear between ELMs and the onset occurs when the temperature gradient threshold is reached [30]. With observations of QCFs between ELMs on C-Mod and DIII-D, the onset of which is due to the temperature gradients, future work should focus on a comparison with existing nonlinear global gyrokinetic calculations in the pedestal region.
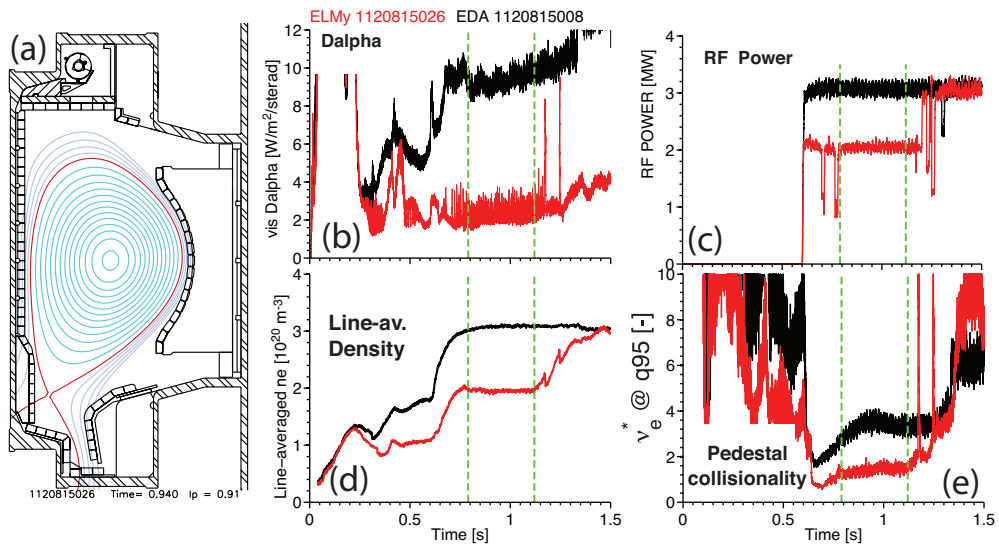
Acknowledgments

Figure 1: (color online) Experimental description. (a) Example of plasma shape to obtain type I ELMy discharges. Times evolution of plasma parameters and comparison between ELMy and EDA H-modes discharges. (b) Characteristics D_α traces. (c) ICRF power traces. (d) The line-averaged density is reduced in ELMy discharges. (e) Reduction of the pedestal collisionality to achieve ELMy discharges.
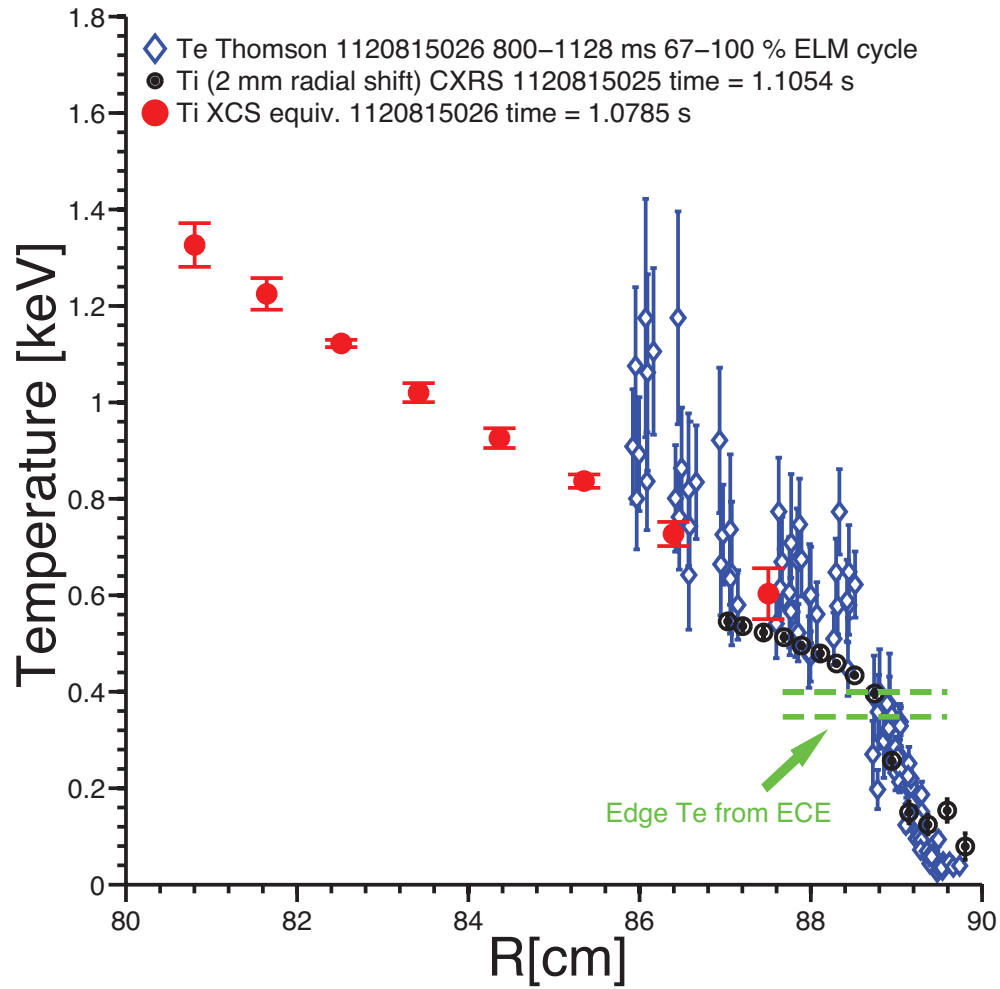
Figure 2: (color online) Radial profiles of the ion and electron temperatures. The blue diamonds represent the electron temperature as measured by the edge Thomson scattering system during the last part of the ELM cycle. The red dots indicate the ion temperature as measured by the XCS system. The black dots represent the edge ion temperature as measured by the CXRS system.
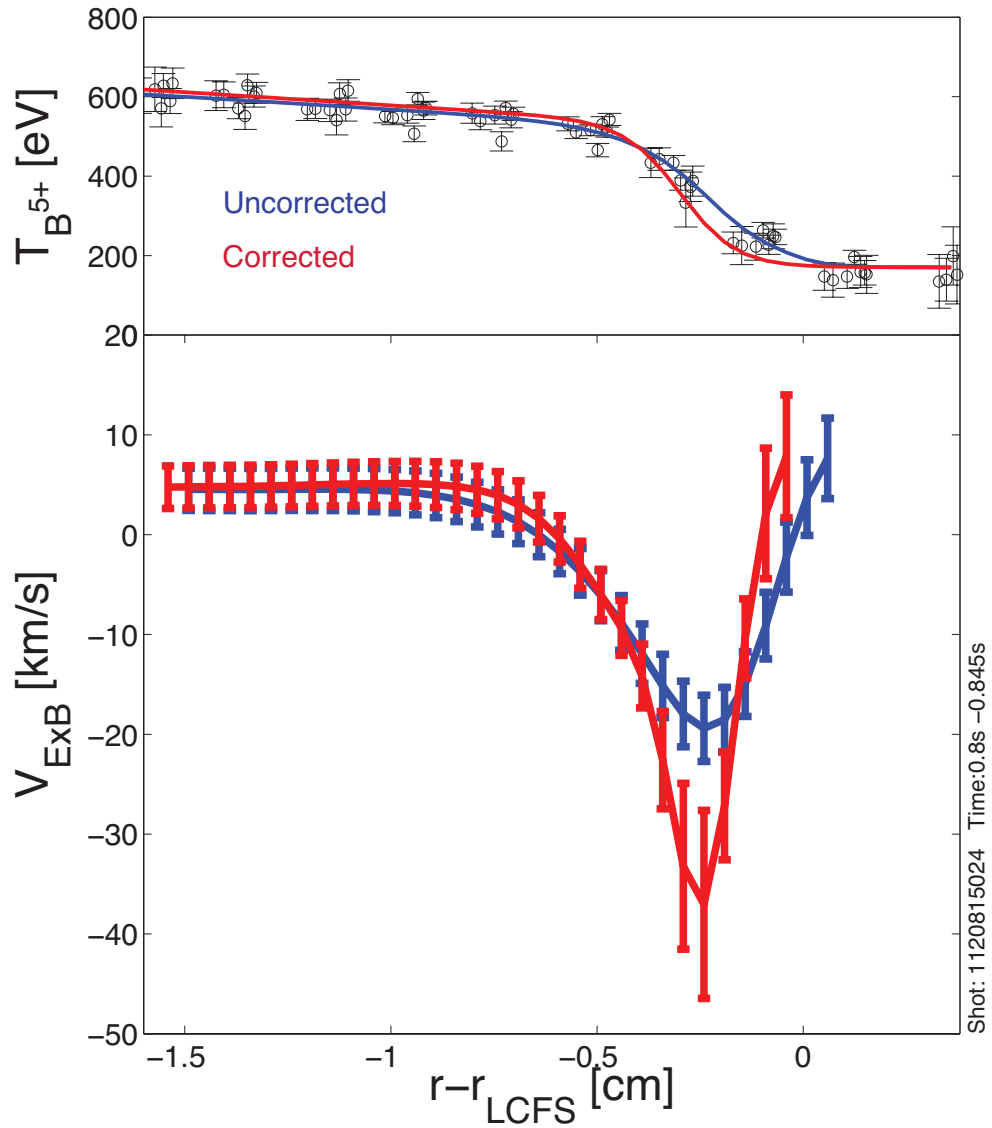
Figure 3: (color online) Top panel: Uncorrected and corrected B^{5+} radial temperature profiles. Bottom panel: Uncorrected and corrected ExB velocity profiles
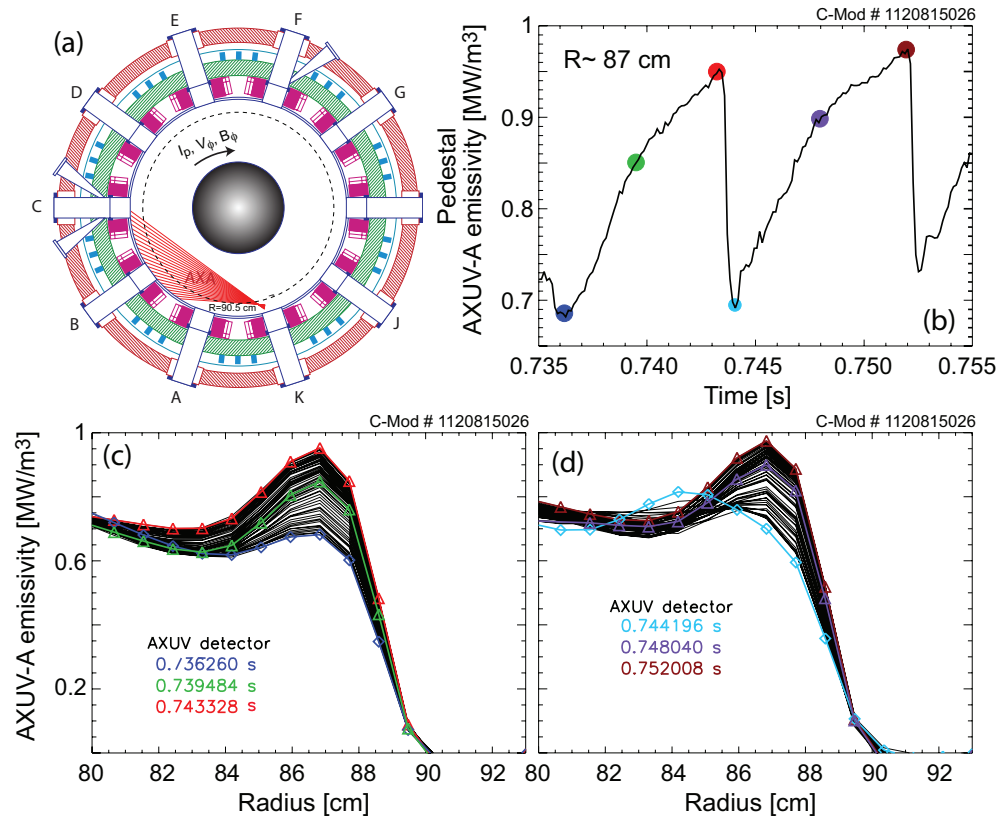
Figure 4: (color online) Intrinsic impurity radiation evolution between ELMs. (a) Top view of the AXA line of sights. (b) Pedestal emissivity temporal evolution between ELMs. Note that impurity emissivity increases monotically until the onset of the next ELM. (c)-(d) Emissivity radial profiles for two inter-ELM phases.
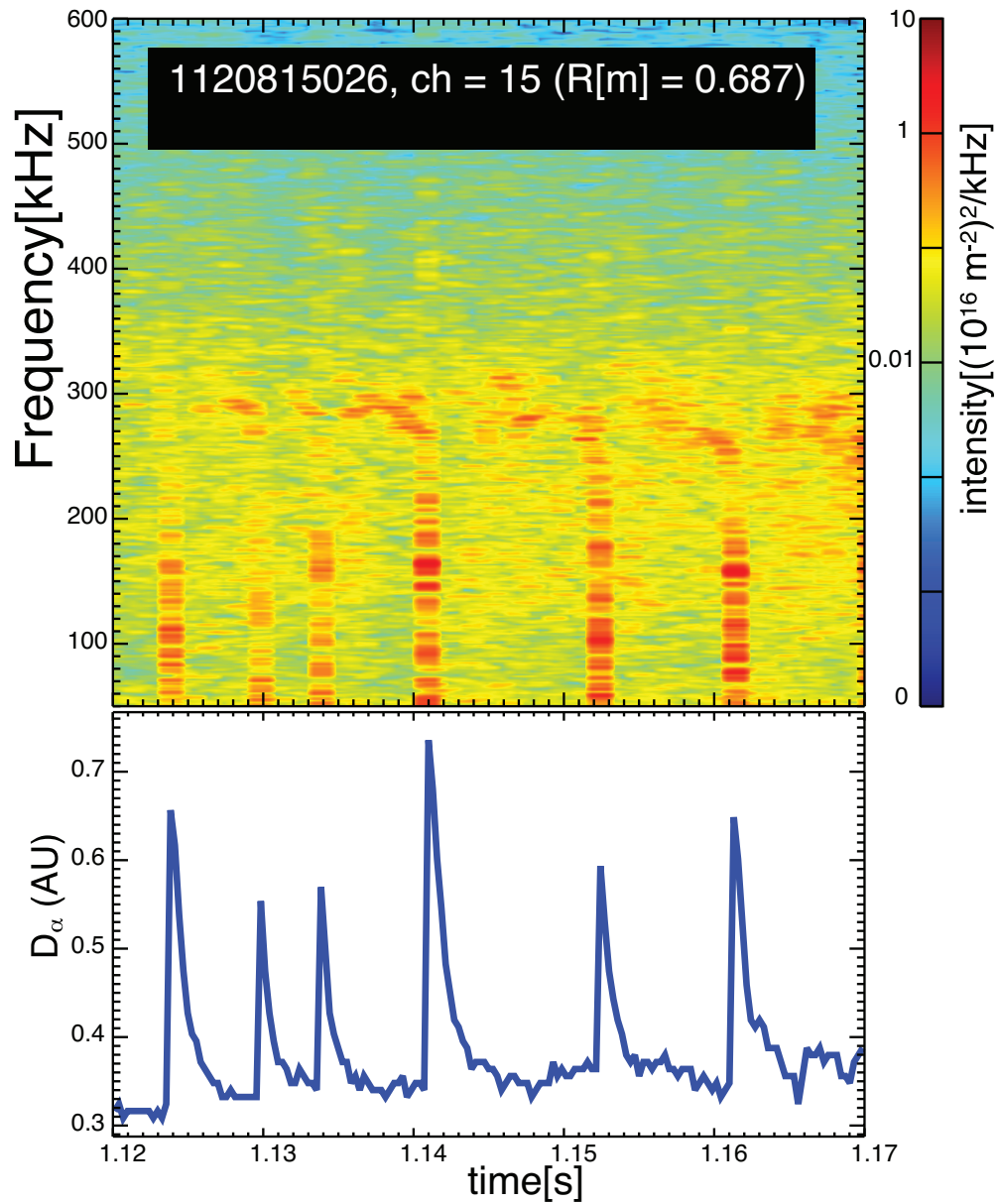
Figure 5: (color online) Inter-ELM PCI fluctuations: Top: Example of PCI spectrogram with coherent fluctuations between ELMs. The bottom panel displays the associated time history of the D_α trace.
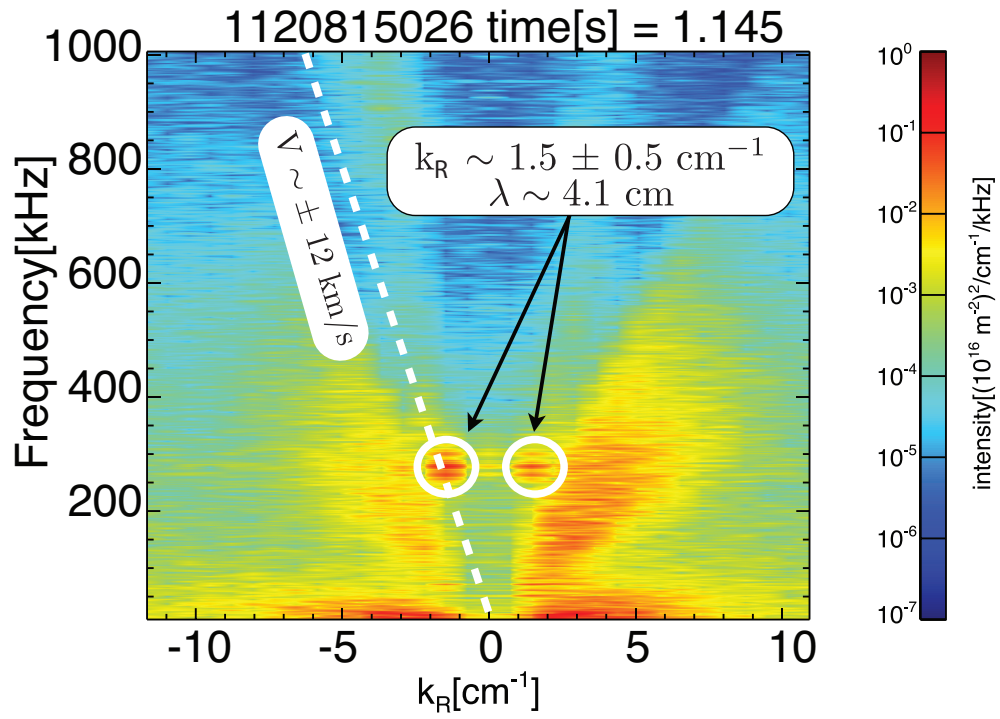
Figure 6: (color online) Frequency-wavenumber spectrum. Two peaks in frequency and wavenumber are highlighted and estimate of the phase velocity is provided.
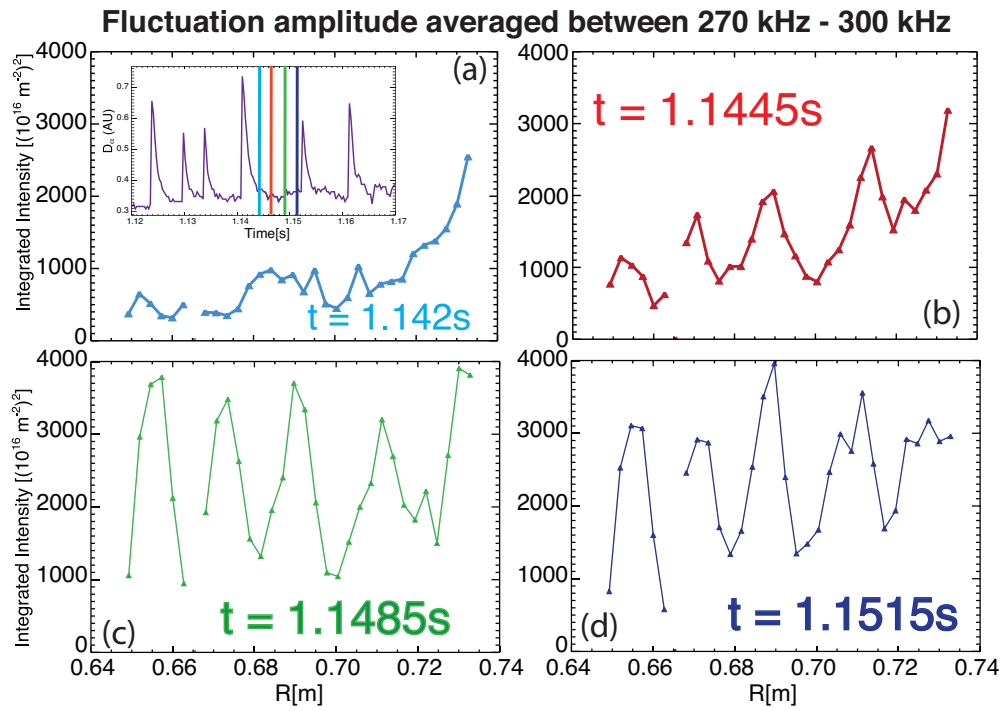
Figure 7: (color online) PCI measurements analysis of the inter-ELM fluctuations amplitude's evolution between 270 kHz and 300 kHz. (a) Radial profile of the amplitude with inset the inter-ELM key for the following radial profiles (b)- through- (d). Note that the corresponding channel at R = 0.665 m is dead, hence the lack of signal.
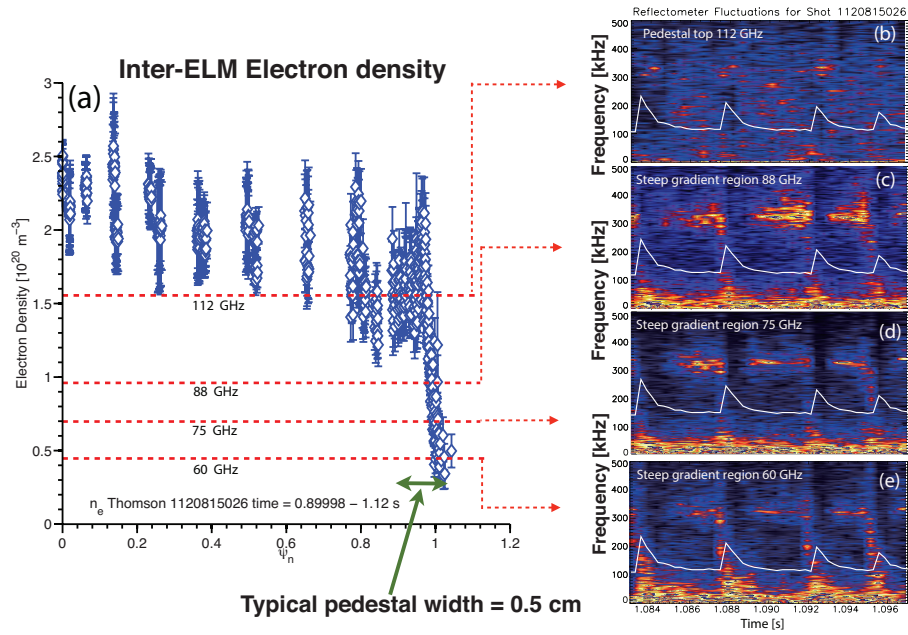
Figure 8: (color online) O-Mode reflectometry. (a) Electron density profile as a function of normalized poloidal flux. Overlayed are horizontal lines indicating the O-Mode reflectometer cutoffs and displayed typical pedestal width. (b) - (e) Inter-ELM spectrograms for various cutoff layers showing the quasi-coherent fluctuations. On each spectrograms, the white trace represents the D_α trace.
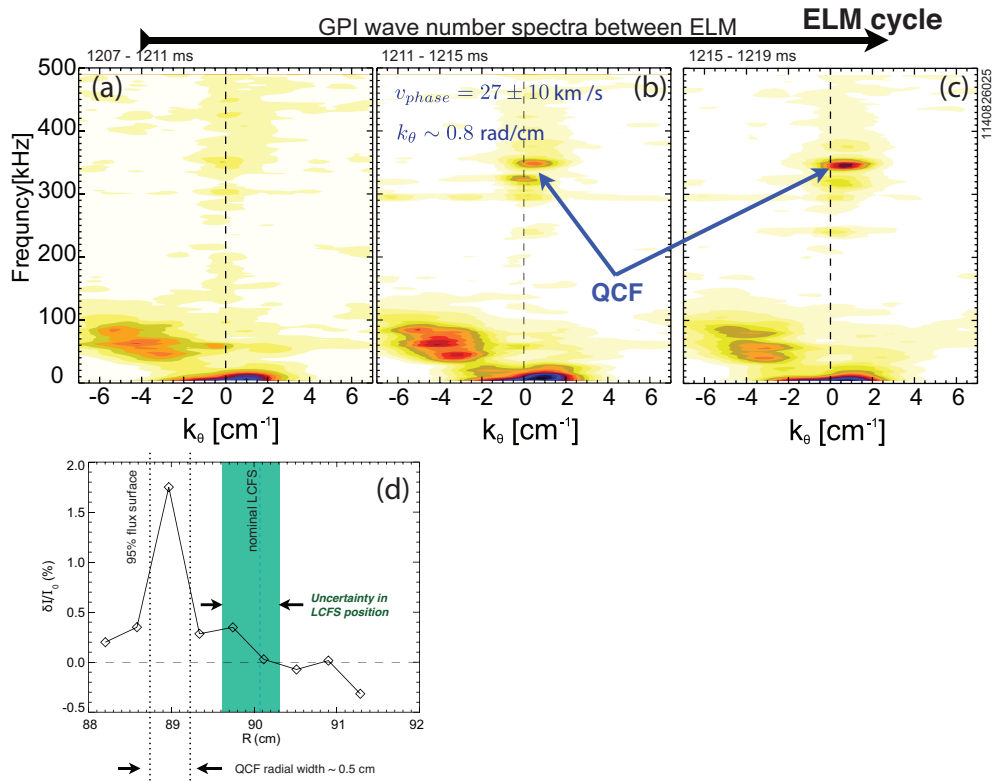
Figure 9: (color online) Gas-Puff imaging (GPI) spectral analysis. (a) -(c) Wavenumber-frequency spectra of the 2D GPI fluctuations during the inter-ELM phase. QCF appears later in the ELM cycle as shown in (b) - (c). Spectral power of the mode as a function of radii is given in (d). The mode layer appears to be 5 mm width with uncertainty relative to the separatrix.
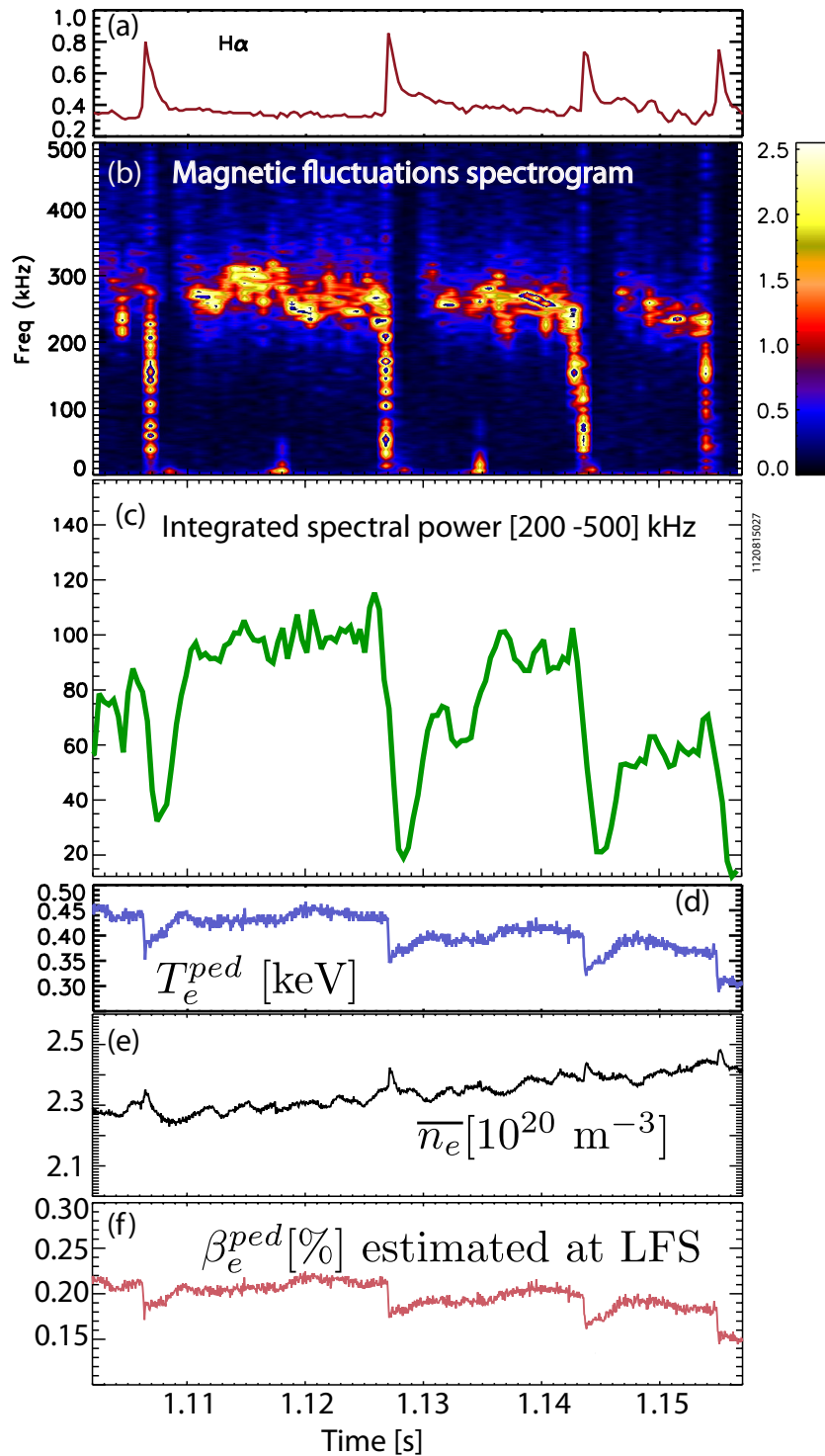
Figure 10: (color online) (a) H_α trace indicates the ELMs (b) Magnetic fluctuations spectrogram displaying the inter-ELM fluctuations sustained for 10 - 20 ms. (c) Integrated spectral amplitude obtained from integrating the above spectrogram between 200 and 500 kHz. (d) Edge temperature evolution measured using the ECE. (e) Line-averaged density evolution. (f) Estimate of the pedestal electron β_e evolution.
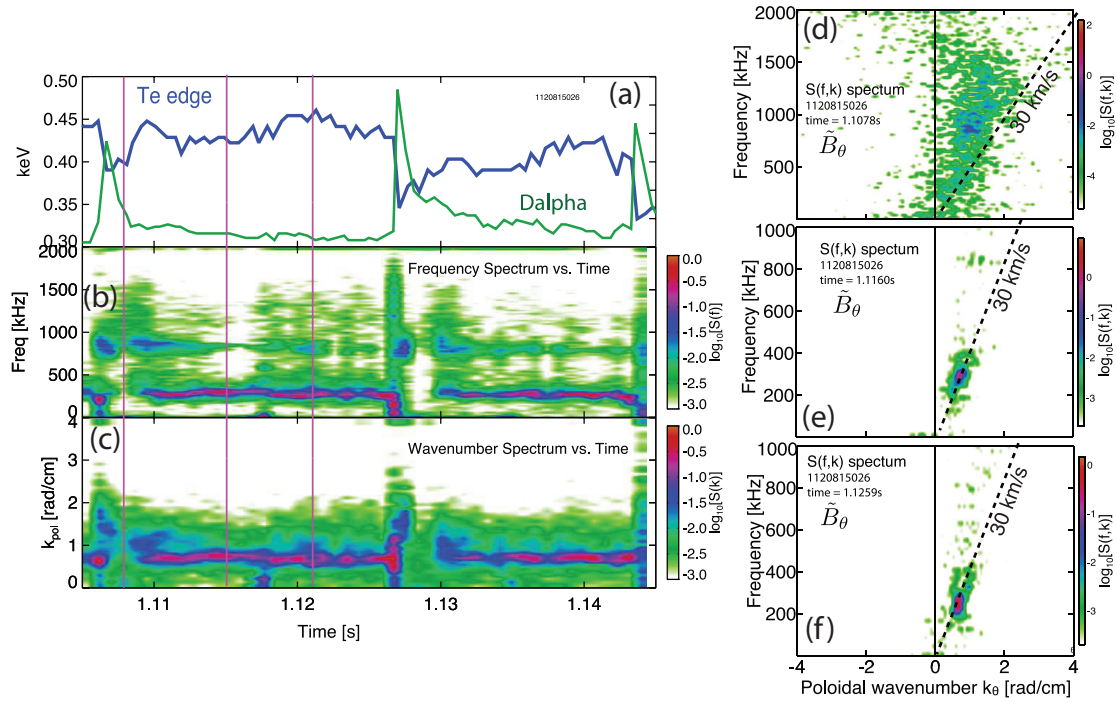
Figure 11: (color online)(a) Time history of the edge temperature as measured using ECE and of the D_{α}. Double head magnetic probe frequency (b) and (c) wavenumber spectrograms. The vertical lines indicate the time slices for which S(k,f) – wavenumber-spectrum– is displayed in (d) through (f).
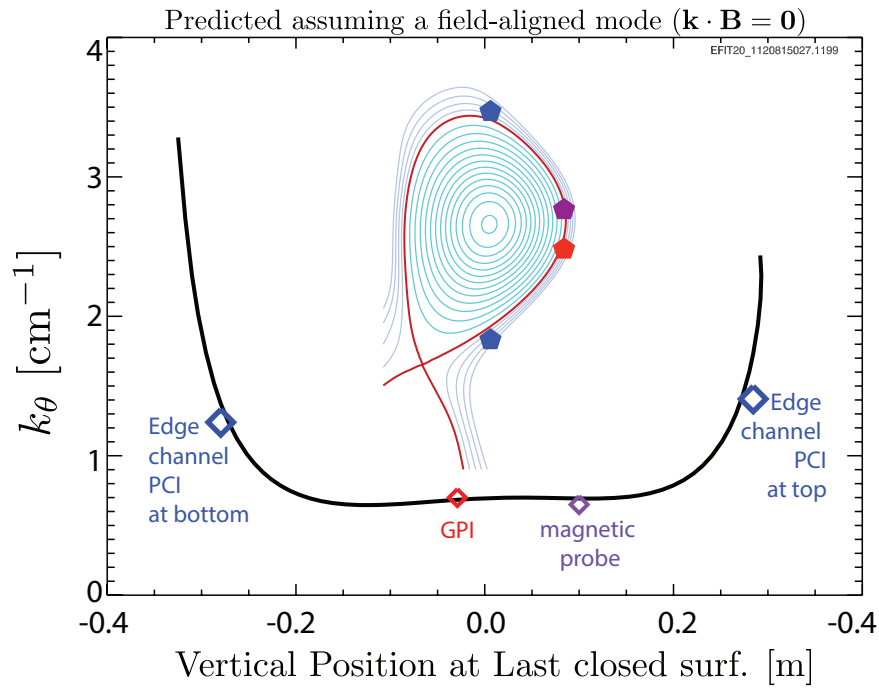
Figure 12: (color online) Predictions of the poloidal wavenumber as a function of the vertical position assuming that the instability is field-aligned. Overlayed are the vertical positions of the different diagnostics used in this work to show agreement in wave numbers. Inset is displayed the flux contour showing the measurement location of each diagnostic.
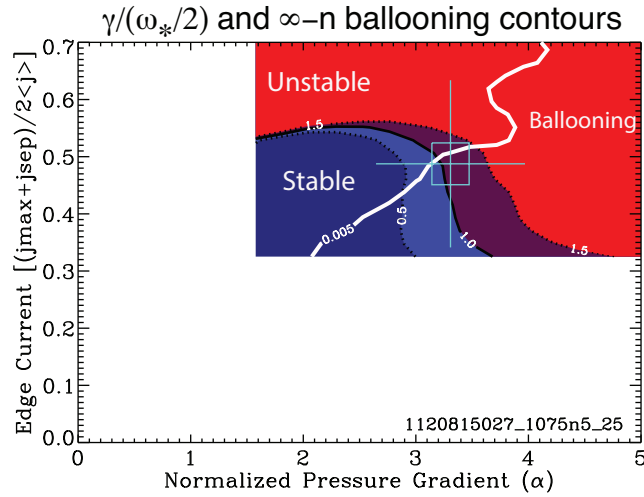
Figure 13: (color online) Peeling ballooning stability (colored contours) and infinite-n ballooning (white solid and dotted line) results. The horizontal axis is the normalized pedestal pressure gradient (MHD alpha parameter) while the vertical axis is peak edge current density normalized by twice the volume-averaged current density. The discharge operating point is shown by the box with error bars. Blue represents the stable region and red the unstable region. Within error bars, the operating point is on the ballooning stability boundary. In addition to the stability calculations using ELITE, the infinite-n ballooning calculation (a proxy for KBM stability) is shown here. The thick white line indicates the 0.5% of the entire poloidal flux, which represents substantial fraction of the edge barrier. The operating point is also infinite-n unstable.
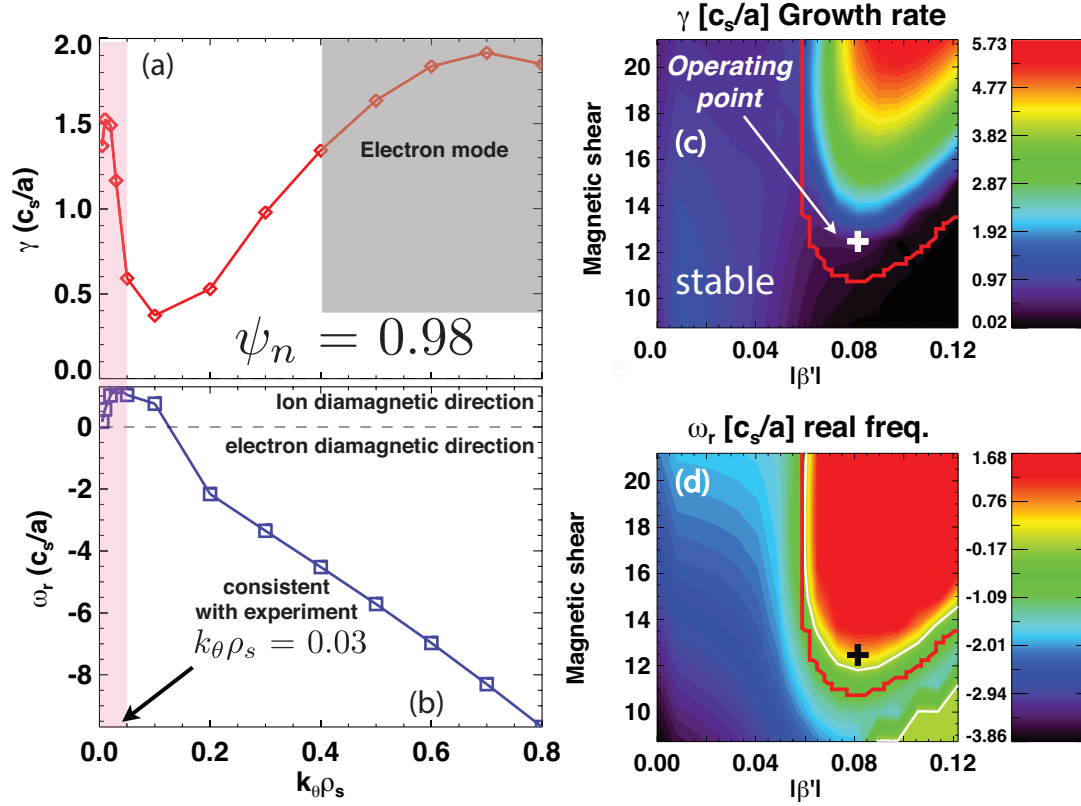
Figure 14: (color online) Local linear GS2 calculations in the steep gradient region $\psi_n = 0.98$. (a) Growth rate as a function of $k_\theta \rho_s$ has two peaks indicating two dominant modes. The peak at low $k_\theta \rho_s \sim 0.03$ is highlighted in red, while the higher $k_\theta \rho_s$ is shown grey. (b) Real frequency with positive indicating ion diamagnetic propagation. The growth rate as function of the pressure gradient β' and magnetic shear is displayed in (c). The operating point lies in the unstable region. The red line near this operating point is the infinite-n ballooning stability line. In (d) the associated real frequency is given.

[1] KINSEY, J., STAEBLER, G., CANDY, J., WALTZ, R., and BUDNY, R., Nuclear Fusion **51** (2011) 083001.
[2] SNYDER, P., GROEBNER, R., HUGHES, J., et al., Nuclear Fusion **51** (2011) 103016.
[3] WALK, J., SNYDER, P., HUGHES, J., et al., Nuclear Fusion **52** (2012) 063011.
[4] DICKINSON, D., SAARELMA, S., SCANNELL, R., et al., Plasma Physics and Controlled Fusion **53** (2011) 115010.
[5] DICKINSON, D., ROACH, C. M., SAARELMA, S., et al., Phys. Rev. Lett. **108** (2012) 135002.
[6] CANIK, J., GUTTENFELDER, W., MAINGI, R., et al., Nuclear Fusion **53** (2013) 113016.
[7] YAN, Z., MCKEE, G. R., GROEBNER, R. J., et al., Phys. Rev. Lett. **107** (2011) 055004.
[8] YAN, Z., MCKEE, G. R., GROEBNER, R. J., et al., Physics of Plasmas **18** (2011) 056117.
[9] GROEBNER, R., CHANG, C., HUGHES, J., et al., Nuclear Fusion **53** (2013) 093024.
[10] DIALLO, A., HUGHES, J. W., GREENWALD, M., et al., Phys. Rev. Lett. **112** (2014) 115001.
[11] MARMAR, E. and GROUP, A. C.-M., Fusion Sci. Tech. **51** (2007) 261.
[12] WUKITCH, S. J., LIN, Y., PARISOT, A., et al., Physics of Plasmas **12** (2005) 056104.
[13] HUGHES, J. W., MOSSESSIAN, D., ZHUROVICH, K., et al., Review of Scientific Instruments **74** (2003) 1667.
[14] REINKE, M. L., PODPALY, Y. A., BITTER, M., et al., Review of Scientific Instruments **83** (2012) 113504.
[15] CHURCHILL, R. M., THEILER, C., LIPSCHULTZ, B., et al., Review of Scientific Instruments **84** (2013) 093505.
[16] P. J. OShea, A. E. Hubbard, Alcator C-Mod Group, in Proceedings of 9th Joint Workshop on ECE and ECRH (Borrego Springs, CA, 1995) J. Lohr, ed. (1995),(p. 7) 1995.
[17] GREENWALD, M. and GROUP, A. C.-M., Fusion Sci. Tech. **51** (2007) 266.
[18] THEILER, C., Spatial resolution of the edge cxrs system on c-mod, Alctor C-Mod Seminar, 2013.
[19] REINKE, M. L. and HUTCHINSON, I. H.
[20] REINKE, M., WHYTE, D., GRANETZ, R., and HUTCHINSON, I., Nuclear Fusion **48** (2008) 125004.
[21] WADE, M. R., BURRELL, K. H., HOGAN, J. T., et al., Physics of Plasmas (1994-present) **12** (2005) .
[22] PORKOLAB, M., ROST, J. C., BASSE, N., et al., IEEE Transactions on Plasma Science **34** (2006) 229.
[23] DOMINGUEZ, A., *Study of density fluctuations and particle transport at the edge ofI-mode plasmas*, PhD thesis, MIT, 2012.
[24] CZIEGLER, I., TERRY, J. L., HUGHES, J. W., and LABOMBARD, B., Physics of Plasmas **17** (2010) 056120.
[25] PUESCHEL, M. J., KAMMERER, M., and JENKO, F., Physics of Plasmas (1994-present) **15** (2008) .
[26] SNYDER, P. B. and HAMMETT, G. W., Physics of Plasmas (1994-present) **8** (2001) 744.
[27] GUTTENFELDER, W., PETERSON, J., CANDY, J., et al., Nuclear Fusion **53** (2013) 093022.
[28] SNYDER, P., *Gyrofluid Theory and Simulation of Electromagnetic Turbulence and Transport in Tokamak Plasmas*, PhD thesis, Princeton University, 1999.
[29] PEREZ, C. P., KOSLOWSKI, H. R., HENDER, T. C., et al., Plasma Physics and Controlled Fusion **46** (2004) 61.
[30] DIALLO, A. and ET. AL., to be submitted to Physics of Plasmas (2014).